Research Square

Preprints are preliminary reports that have not undergone peer review.
They should not be considered conclusive, used to inform clinical practice,
or referenced by the media as validated information.

Simultaneous transformation of lignocellulosic components using acidic deep eutectic solvents: From action mechanism to scale extraction

Dengfeng wang
Zhejiang Provincial Innovation Center of Advanced Textile Technology
Haojie Hong
Zhejiang Sci-Tech University
Han Wu
Zhejiang Sci-Tech University
Lin Liu
linliu@zstu.edu.cn

Zhejiang Sci-Tech University
Juming Yao
Zhejiang Sci-Tech University

Research Article

Keywords: Lignin, lignocellulosic nanofibrils, solvent–biomass interactions, acidic deep eutectic solvents, scalable validation

Posted Date: November 9th, 2026

DOI: https://doi.org/10.21203/rs.3.rs-10323768/v1

License: This work is licensed under a Creative Commons Attribution 4.0 International License.
Read Full License

Additional Declarations: No competing interests reported.

Simultaneous transformation of lignocellulosic components using acidic deep eutectic solvents: From action mechanism to scale extraction

Dengfeng wang[b], Haojie Hong[a,b], Han Wu[a], Lin Liu[a,b,*], Juming Yao [a,*]

[a] *State Key Laboratory of Bio-based Fiber Materials, School of Materials Science and Engineering, Zhejiang Sci-Tech University, Hangzhou 310018, China*

[b] *Zhejiang Provincial Innovation Center of Advanced Textile Technology, Shaoxing, 312000, China*

* Corresponding author: Professor Lin Liu

Email address: linliu@zstu.edu.cn (L. Liu)

Tel: +86-571-86843618

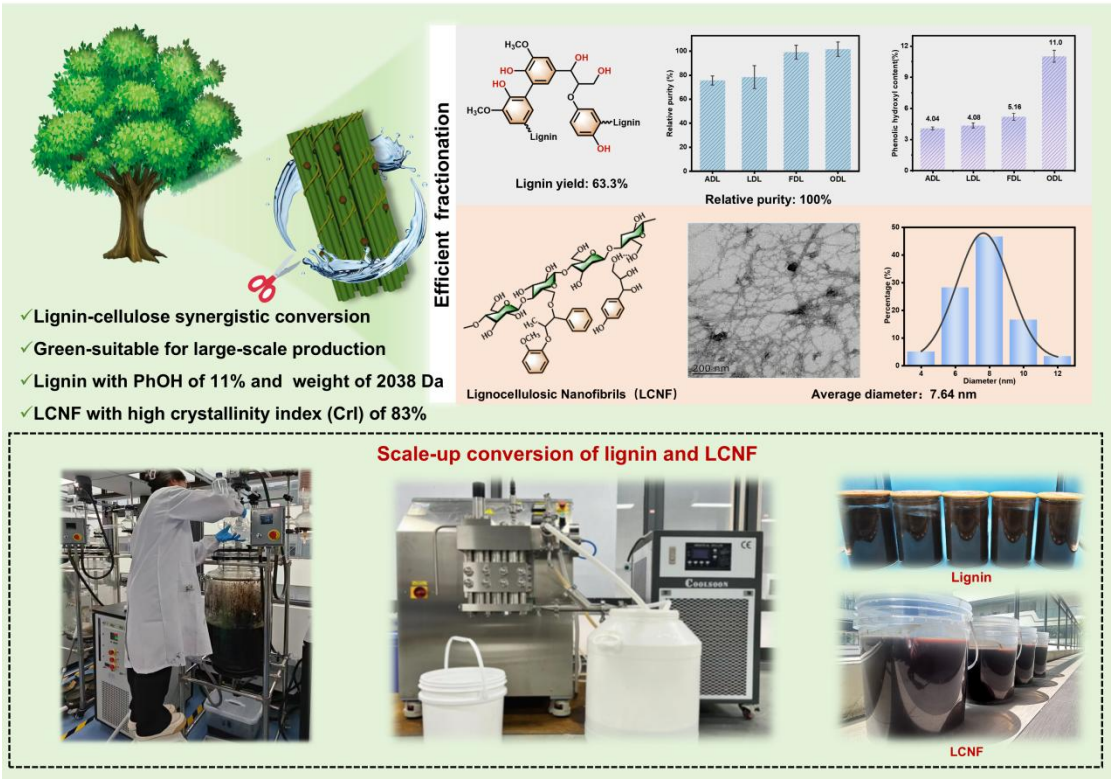
Professor Juming Yao

Email address: yaoj@zstu.edu.cn (JM. Yao)

Abstract: Achieving the balanced valorization of lignocellulosic components is essential for improving atom economy and sustainability in biorefinery, yet remains challenging. Herein, a green and scalable strategy was developed for the synergistic conversion of lignocellulosic biomass to polyphenoliclignin and lignocellulosic nanofibers (LCNFs) using customized acidic deep eutectic solvents (DESs). The acidity and hydrogen-bonding capability of the designed DESs were regulated by altering the hydrogen bond donors, including formic, acetic, lactic, and oxalic acids. Kamlet-Taft solvatochromic analysis and DFT calculations showed that the oxalic acid-based DES (OD) had the strongest hydrogen-bonding ability (β= 3.340) and acidity (α= 1.882). This efficiently disrupted the hydrogen-bonding network and selectively cleaved lignin ether bonds and glycosidic bonds in amorphous cellulose. Consequently, LCNFs with a high crystallinity index (CrI) of 83% and an average diameter of 7.64 nm were obtained. Simultaneously, high-quality lignin (ODL) was produced with a yield of 63.3%, phenolic hydroxyl content of 11%, nearly 100% purity, and a low molecular weight of 2038 Da. Structural characterization revealed that ODL exhibited substantially reduced *β-O-4* and *β-β* linkages, with guaiacyl (G) and syringyl (S) units accounting for 54.5% and 44.3%, respectively, demonstrating the selective cleavage and structural regulation of lignin by acidic DESs. Furthermore, the DES system was successfully scaled up to a processing capacity of 100 kg lignocellulose per day. This work provides a scalable and mechanistically informed platform for the integrated production of high-purity lignin and LCNFs from lignocellulosic biomass.

Keywords: Lignin, lignocellulosic nanofibrils, solvent–biomass interactions, acidic deep eutectic solvents, scalable validation

Graphical abstract



1. Introduction

Lignocellulose, the most abundant renewable biomass resource, has attracted considerable attention as a sustainable feedstock because of its carbon neutrality, low cost, and wide availability [1-3]. However, efficient valorization of lignocellulose remains challenging due to its complex hierarchical structure, in which cellulose, hemicellulose, and lignin are interconnected through extensive hydrogen bonding and covalent interactions, forming a stable lignin-carbohydrate complex (LCC) architecture. This intrinsic recalcitrance severely restricts selective component separation and high-value conversion. Various deconstruction strategies, including organosolv fractionation [4-6], hydrothermal treatment [7], acid/alkali treatment [8, 9], and enzymatic hydrolysis [10, 11], have been developed to overcome biomass recalcitrance. These approaches generally rely on strong physicochemical or biochemical driving forces to disrupt lignocellulose structures by cleaving lignin C-O/C-C bonds, breaking lignin-carbohydrate linkages, and weakening hierarchical supramolecular networks. However, owing to the distinct chemical and structural features of lignin and carbohydrates, current fractionation strategies are typically designed toward lignin-first or cellulose-first conversion pathways [12, 13]. Thermochemical processes facilitate lignin depolymerization but often suffer from lignin condensation and uncontrolled degradation, whereas enzymatic hydrolysis provides excellent selectivity but mainly enables component-specific conversion, limiting the valorization of associated fractions. Therefore, developing selective deconstruction strategies capable of achieving balanced and synergistic conversion of multiple lignocellulosic components remains highly desirable.

Deep eutectic solvents (DESs) have emerged as promising media for lignocellulose biorefinery due to their tunable composition, environmental compatibility, and facile synthesis [14-16]. By rationally selecting hydrogen bond donor (HBD) and hydrogen bond acceptor (HBA) pairs, the hydrogen-bonding capability, polarity, acidity, and chemical reactivity of DESs can be precisely regulated, thereby enabling selective interactions with specific lignocellulosic components. For instance, Liu et al. demonstrated that tailoring HBD components and functional groups effectively modulated the hydrogen-bonding ability and polarity of

DESs, strengthening DES-lignin interactions and achieving lignin dissolution efficiency of 48.6 wt%. Conversely, Wang et al. [17] designed cholinium-amino acid based DES systems through compositional regulation, enabling preferential carbohydrate deconstruction. The optimized DESs achieved 44.6-62.1% hemicellulose removal with only 23.6-36.8% lignin removal, demonstrating that DES composition plays a critical role in governing fractionation selectivity and the structural characteristics of the resulting biomass fractions. These studies highlight the critical role of DES composition in directing lignocellulose fractionation selectivity and conversion pathways.

Among various DES formulations, acidic DESs have attracted particular attention due to their strong proton-donating capability and catalytic activity toward lignocellulose deconstruction. Our previous work [18] revealed that acidic DESs could simultaneously disrupt hydrogen-bond networks and promote nucleophilic cleavage of aryl ether bonds, enabling efficient lignin extraction with high purity, enhanced reactivity, and reduced molecular weight. Furthermore, a betaine/oxalic acid-based DES system was demonstrated to regulate cellulose structures through acid-assisted hydrogen-bond network disruption, improving cellulose accessibility and facilitating subsequent nanofibrillation. The resulting cellulose nanofibrils exhibited an average diameter of 43.7±21.7 nm and a high aspect ratio of 24.6 [19]. Collectively, these findings demonstrate that acidic DESs provide a versatile platform for regulating lignocellulose depolymerization selectivity. However, the fundamental relationship between DES acidity, molecular interactions, and balanced lignocellulose conversion remains insufficiently understood. Furthermore, the rational optimization of acidic DES systems and their scalability toward practical applications remain challenging.

In this work, an acidity-regulated DES strategy was developed to optimize solvent-lignocellulose interactions, enabling the integrated conversion of lignin and cellulose fractions. By regulating hydrogen bond donors (formic, acetic, oxalic, and lactic acids), the physicochemical properties of DESs were tailored, and the choline chloride-oxalic acid (OD) exhibited enhanced hydrogen-bonding competitiveness and proton-donating capability. This optimized DES system effectively disrupted LCC

structures through competitive hydrogen-bond interactions, while promoting selective cleavage the ether bond in lignin and glycosidic bonds in cellulose amorphous regions. Consequently, phenolic hydroxyl-rich lignin and cellulose nanofibrils with preserved crystalline structures were simultaneously obtained. The yield, purity, structural characteristics, and physicochemical properties of the resulting fractions were systematically investigated to elucidate the mechanisms underlying the synergistic transformation of lignocellulosic components. Based on the 100 kg-scale scale-up trial, the practicality and scale-up feasibility of the process under this synergistic conversion strategy were verified. This work provides mechanistic insights into acidity-regulated DES design and establishes a scalable strategy for integrated lignocellulose valorization.

2. Experimental

2.1 Materials

Poplar sawdust (Guilin Thousand Bamboo Workshop Bamboo Industry Co., Ltd., Guangxi), Choline chloride (ChCl), Formic acid (FA), Acetic acid (AA), Lactic acid (LA), Oxalic acid (OA), Nile Red, 4-nitroaniline, 4-nitroanisole, Methanol (CH_3OH), Acetyl bromide, Tetrahydrofuran, 1,4-dioxane, NaOH, Monosodium phosphate, Disodium phosphate, and d_6-DMSO were all purchased from Macklin Reagent and used directly without purification.

2.2 Synthesis of DES

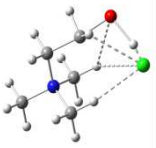
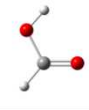
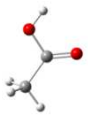
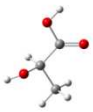
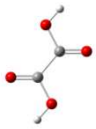
Four deep eutectic solvents (DESs) were prepared by mixing ChCl as HBA withFA, AA, LA, and OA as HBDs at the molar ratios specified in Table 1. The mixtures were stirred at 300 rpm at 80 °C until homogeneous and transparent solutions formed. The resulting DESs were designated as FD, AD, LD, and OD, respectively (Table 1).

2.3 Depolymerization of poplar sawdust

The prepared DES was mixed with poplar sawdust at a mass ratio of 15:1, and the mixture was depolymerized at 100 °C for 6 h. After pretreatment, the depolymerized mixture was negative pressure filtered through 0.45 μm neutral filter paper to separate the liquid and solid products. The crude lignin was then washed with 10% ethanol/water solution, filtered, and dried to afford the purified lignin. The

residual solid samples were collected and washed with 10% ethanol/water solution to remove impurities. The washed lignocellulosic solid residue was dispersed in water at a volume ratio of 1:100, and then subjected to homogenization for five cycles to obtain LCNF. The designations of all samples are listed in Table 1.

Table 1. Composition of DESs, pKa of HBDs and nomenclature

Composition			pKa of HBD	Nomenclature		
HBA	HBD	Molar ratio（HBA/HBD）		DES	Lignin	Residual solid
 ChCl	 FA	1:2	3.75	FD	FDL	FDR
	 AA	1:2	4.76	AD	ADL	ADR
	 LA	1:2	3.86	LD	LDL	LDR
	 OA	1:1	1.23	OD	ODL	ODR

3. Results and Discussion

3.1 Physicochemical properties and solvent effects of DES

With reference to the Kamlet-Taft solvatochromic parameters [20, 21], the absorbances of DES at different peak wavelengths were measured in three dyes: Nile red (NR, 550-650 nm), 4-nitroaniline (NH_2, 300-450 nm), and 4-nitroanisole (OMe, 300-350 nm). As shown in Figure S1 and Figure 1a, calculated by Equations (1-3), AD exhibited the strongest hydrogen bond accepting ability (β= 3.340), indicating a weak proton-donating ability of this system and consequently a low hydrogen bond

acidity (α= 1.204). Notably, OD exhibited the highest hydrogen bond acidity (α=1.882) among the tested DESs, indicating its strongest hydrogen bond donor capacity, which is favorable for the competitive disruption of intermolecular and intramolecular hydrogen bonds in lignocellulose.

$$\alpha = \frac{19.9567 - 1.024\pi^{*} - \nu_{NR}}{1.6078} \quad (1)$$

$$\beta = \frac{1.035\nu_{OMe} + 2.64 - \nu_{NH_2}}{2.80} \quad (2)$$

$$\pi^{*} = \frac{34.12 - \nu_{OMe}}{2.343} \quad (3)$$

$\boldsymbol{\alpha}$ represents the hydrogen bond donor ability (hydrogen bond acidity) of the solvent, $\boldsymbol{\beta}$ represents the hydrogen bond acceptor ability (hydrogen bond basicity), $\boldsymbol{\pi^{*}}$ represents the polarizability, $\boldsymbol{\nu}$ represents the maximum absorption wavenumber of the probe molecule in the test solvent (cm^{-1}).

The optimized geometries shown in Figures 1b-e revealed that both Ch^{+} and Cl^{-} participated in hydrogen bonds with the HBDs. Specifically, the carboxyl hydrogens of FD, AD, and LD formed O-H···Cl hydrogen bonds with bond lengths of 2.061-2.073, 2.080-2.100, and 2.070-2.076 Å, respectively, while OD exhibited the shortest O-H···Cl distance of 1.908 Å, corresponding to the strongest hydrogen-bonding interaction. This was primarily attributed to the dicarboxylic structure of OD, which provides additional hydrogen-bonding sites and a more concentrated charge distribution, thus enhancing its hydrogen bonding capacity with chloride ions. Additionally, the strong hydrogen-bond interaction induces an electron delocalization effect, which contributes to the enhanced acidity of OD-based DESs, consistent with its highest α value.

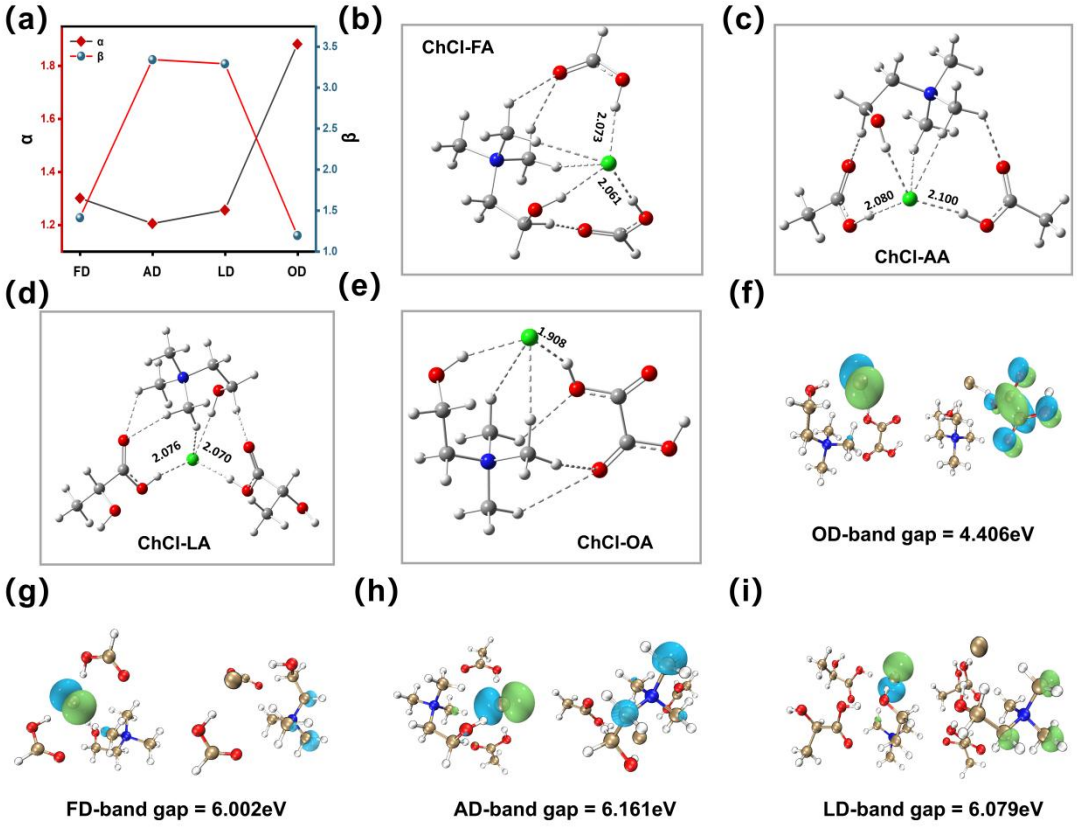


Figure 1. FD, AD, LD, and OD of α and β values (a), atomic distances (b-e), and band gaps (f-i).

Furthermore, the LUMO-HOMO orbitals of the four DESs were calculated using Gaussian DFT to evaluate their reactivity [22]. As shown in Figures 1f-i, the HOMO-LUMO band gaps were 6.002 eV for ChCl-FA, 6.161 eV for ChCl-AA, 6.079 eV for ChCl-LA, and 4.406 eV for ChCl-OA. Among them, OD exhibited the smallest band gap (4.406 eV), indicating that less energy was required for electronic transitions and suggesting potentially higher reactivity. This result was consistent with the aforementioned analysis of hydrogen bond acidity and the molecular structure optimization. The charge distribution in the hydrogen-rich network DESs was studied through the molecular surface electrostatic potential analysis, in which the red regions denote strongly electropositive sites, the dark blue regions indicate strongly electronegative sites, and the white transitional zones correspond to neutral character. As shown in Figures 2a-d, the electrostatic potential ranges for the FD, AD, LD, and OD systems were −43.04 to 42.91, −46.13 to 40.66, −46.66 to 48.33, and −51.32 to 47.11 kcal/mol, respectively. As to quantitative distribution of electrostatic potential, significant differences in electrostatic potential surface area distributions were

observed between the AD and LD systems. In contrast, OD exhibited the strongest negative potential and a more uniform distribution, indicating that it possessed stronger solvation capability and a more stable supramolecular structure. This property is expected to provide a favorable solvation environment for the dissolution and functionalization of lignocellulose.

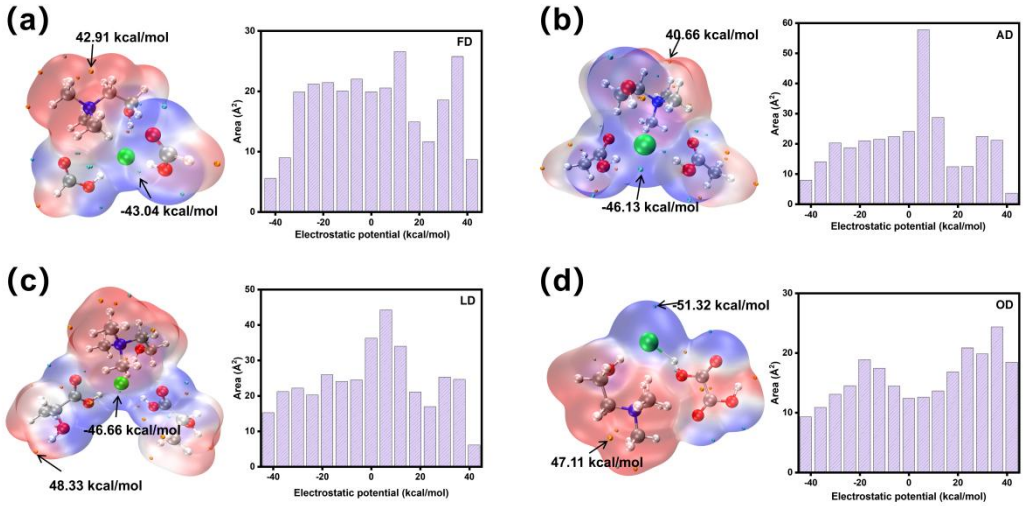


Figure 2. Electrostatic potential distribution and quantitative analysis of molecular surface electrostatic potential for FD (a), AD (b), LD (c), and OD (d).

3.2 Acidic DES-mediated lignin extraction and structural regulation

As illustrated in the schematic diagram of the lignocellulose fractionation process in Figure 3a, poplar sawdust was subjected to depolymerization by four acidic DESs to obtain lignin and lignocellulosic residues. As shown in Figure 3b, lignin extraction yields varied considerably across DES systems: FD, AD, and LD gave only 9.9%, 3.5%, and 3.5%, respectively, whereas OD achieved a markedly higher yield of 63.3%. This efficient delignification was further reflected in the yield of residual solid: OD treatment left only 49.0% of the original wood powder, compared to 73.6%, 86.8%, and 83.3% for FD, AD, and LD, respectively (Figure 3c). Collectively, these trends correlate consistently with the acidity order of the DES systems. The relative purity of the extracted lignin was evaluated by the Klason method. The purities of ADL and LDL were both below 80%, whereas ODL exhibited the highest purity, approaching 100% (Figure 3d). The high yield and high purity of lignin obtained with the OD system can be primarily attributed to its strong acidity and the highest hydrogen bond donor ability, which provides more acidic protons to effectively disrupt the lignin-carbohydrate complex (LCC) structure in lignocellulose, thereby

enabling the high-purity, high-yield separation of lignin. Furthermore, the phenolic hydroxyl contents of ADL, LDL, and FDL were 4.04%, 4.08%, and 5.16%, respectively, whereas ODL exhibited a substantially higher content of 11.0% (Figure 3e). This pronounced improvement was primarily attributed to the greater ionization of oxalic acid, which released more H^+ that protonated the C_α-OH groups of lignin, leading to *β-O-4* bond cleavage and the concomitant formation of new phenolic hydroxyl groups [23].

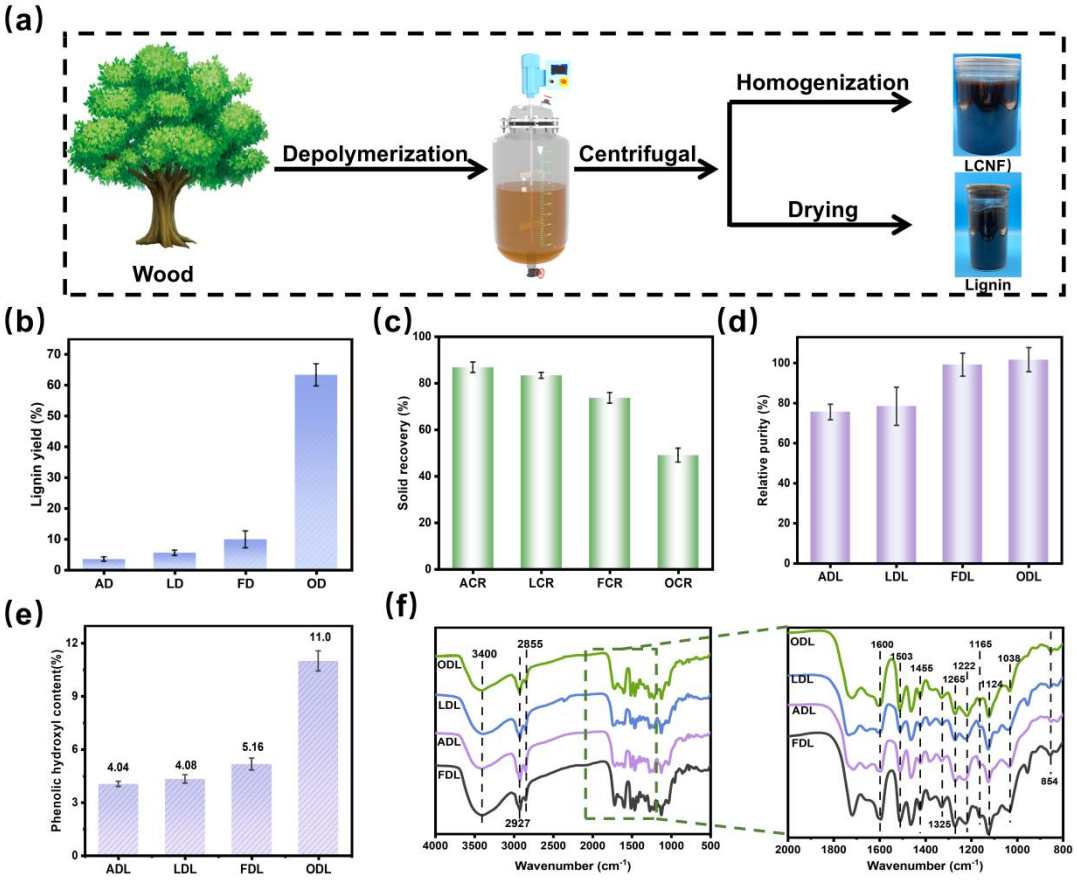


Figure 3. Schematic diagram of the lignocellulose separation and purification in DES systems (a). Yield of various lignin (b) and residual solid (c), relative purity (d), phenolic hydroxyl content (e) and FTIR spectra (f) of different lignin samples.

FTIR spectroscopy was employed for preliminary structural the characterization of the various lignin samples. The FTIR spectra of all lignin samples exhibited similar absorption features (Figure 3f). The absorption bands at 3400, 2927/2855, 1600/1503/1455 cm^{-1} were assigned to stretching vibration of O-H, $-CH_3$/$-CH_2$ and skeletal vibrations of benzene ring. The absorption band at 1724 cm^{-1} was assigned to

the C=O stretching of non-conjugated carbonyl or carboxyl groups, suggesting esterification during lignin extraction. The bands at 1265, 1222, and 1038 cm^{-1} were assigned to guaiacyl (G) units, while those at 1325 and 1124 cm^{-1} originated from syringyl (S) units, collectively confirming that all extracted lignin were predominantly G/S-type structures. Additionally, the weak peak at 1165 cm^{-1} indicated the presence of small amounts of H-type units in all lignin samples.

2D HSQC was used to further analyze the detailed structures of lignin samples. As shown in Figures 4a-d and Table S1, characteristic signals of the *β-O-4*, *β-β*, and *β-5* linkages were detected in all samples. Specifically, the C_α-H_α correlation of *β-O-4* linkages appeared at δC/δH 72.8-71.6/4.89-4.81 ppm; C_β-H_β correlations of *β-O-4* structures attached to guaiacyl (G) and syringyl (S) units appeared at δC/δH 84.1-83.6/4.30-4.26 ppm and 86.5-85.5/4.18-4.03 ppm, respectively, while the C_γ-H_γ correlation was located at δC/δH 59.6-59.5/3.66-3.60 ppm. For *β-β* resinol substructures, the C_β-H_β, C_γ-H_γ, and C_α-H_α correlations were detected at δC/δH 53.5-53.2/3.08-3.03, 71.4-71.2/4.18-3.73, and 85.9-84.1/4.68-4.60 ppm, respectively. The C_α-H_α and C_γ-H_γ correlations of the *β*-5 (phenylcoumaran) substructure appeared at δC/δH 87.9-87.2/5.54-5.42 and 62.4-62.2/3.71-3.70 ppm, respectively [24-26]. Notably, in the ODL sample, several signals in the side-chain region were markedly attenuated, which was attributed to extensive cleavage of side-chain bonds under the strongly acidic DES. Subsequently, the major structural units in lignin were quantified by 2D HSQC NMR. The results were expressed per 100 aromatic units (Ar) and are summarized in Table 2. The relative content of *β-O-4* linkages dropped sharply from 43.0, 41.1, and 37.0 per 100Ar in ADL, LDL, and FDL, respectively, to only 9.7 per 100 Ar in ODL. This acid-driven depolymerization proceeds via protonation of benzylic hydroxyl groups to form carbocation intermediates, which subsequently trigger *β*-aryl ether scission. The reaction is further facilitated on S units due to the higher electron density on aromatic rings. Accordingly, the S/G ratio decreased from 0.51 in ADL to 0.41 in LDL, confirming that the initial mild acidity selectively cleaved S-unit-associated *β-O-4* bonds. With further increases in acidity, the S/G ratio rose from 0.62 of FDL to 1.23 of ODL, indicating that the more acidic DES intensified the release of S-unit-rich fragments. Overall, higher acidity of the DES led

to more extensive cleavage of ether bonds, with the OD system exhibiting the strongest effect.

GPC analysis confirmed that the acidic DES systems induced pronounced depolymerization, leading to markedly reduced molecular weights. As shown in Figure S2, ADL, LDL and FDL possessed weight-average molecular weights (M_w) of 2481, 2457 and 3648 g/mol, respectively, with corresponding polydispersity indices (PDI) of 1.42, 1.46 and 1.48. For the ODL, the combined action of hydrogen-bond competition within the LCC and acid-catalyzed *β*-aryl ether scission synergistically promoted the release of highly homogeneous lignin fragments, as reflected by its particularly low M_w of 2038 g/mol and narrow PDI of 1.31.

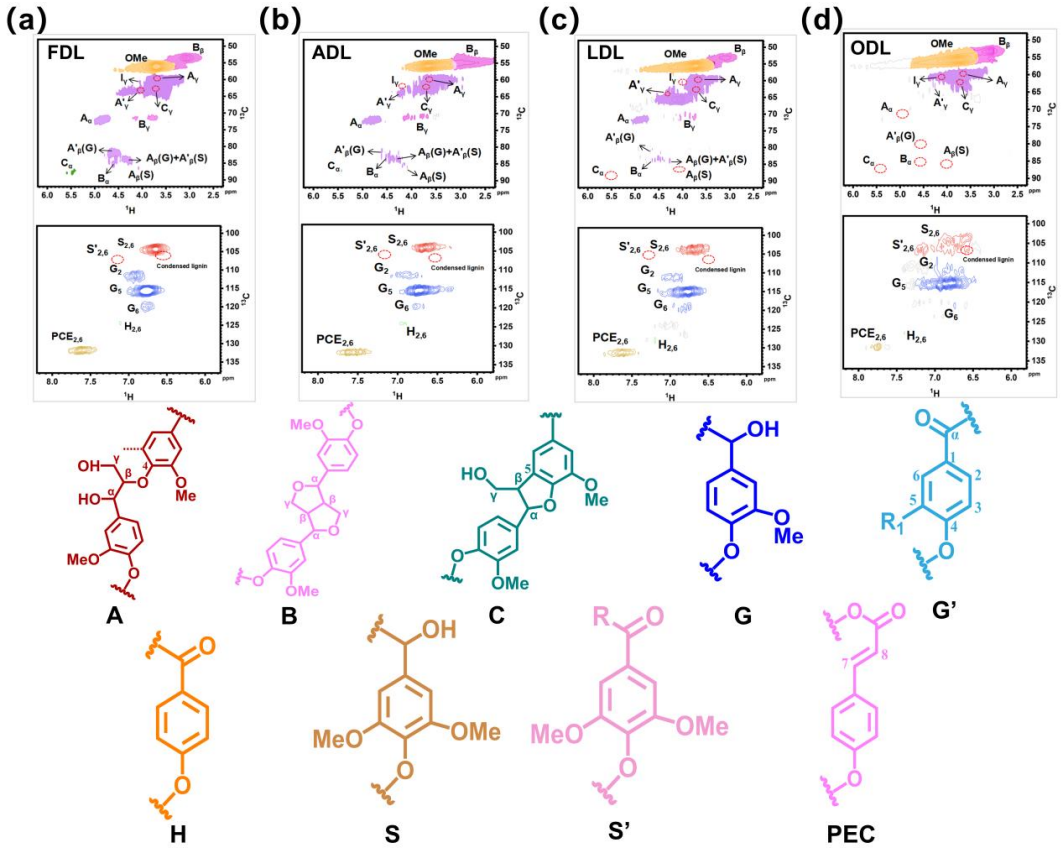


Figure 4. HSQC spectra and related substructures of FDL (a), ADL (b), LDL (c), and ODL (d).

Table 2 Relative abundance of different structural units in lignin samples

Lignin	β-O-4/100Ar	β-β_α/100Ar	β-β_γ/100Ar	S/100Ar	G/100Ar	H/100Ar	S/G
ADL	43.0	4.6	2.7	31.1	61.1	7.8	0.51
LDL	41.1	2.6	1.7	28.4	69.4	2.2	0.41
FDL	37.0	3.6	3.6	37.5	60.6	1.9	0.62
ODL	9.7	0.6	2.5	54.5	44.3	1.3	1.23

3.3 Acidic DES-mediated structural evolution of Lignocellulose residue and LCNF

The morphological and chemical structures of the separated cellulose residues were characterized and analyzed. As shown in Figure S3, the untreated poplar wood powder exhibited a rod-like morphology with a dense and uniform structure. After treatment with FD, AD and LD, the wood surfaces displayed evident etching, yet the overall rod-like shape was largely retained. This indicated that the hydrogen-bond competition exerted by these three DESs was insufficient to fully disrupt the lignin-carbohydrate complex (LCC) structure. In contrast, through the synergistic action of hydrogen-bond competition and acid-catalyzed degradation, OD effectively promoted the depolymerization of lignocellulose and the hydrolysis of cellulose amorphous regions and hemicellulose. This yielding a cellulose residue with a loose, fragmented structure and significantly reduced particle size (Figure 5a).

The FTIR analysis shown in Figure 5b revealed that the characteristic peaks observed in all samples at 3396, 2912, 1433, 1156, and 1058 cm^{-1} were assigned to O-H stretching, -CH_2- asymmetric stretching, C-H shearing, antisymmetric C-O-C bridge stretching, and C-O stretching, respectively. This indicated that the DES treatment did not alter the native cellulose backbone. Meanwhile, the attenuated aromatic skeletal vibrations at 1600 and 1512 cm^{-1} reflected the partial removal of lignin. Furthermore, all cellulose residue samples exhibited a characteristic ester carbonyl peak at 1743 cm^{-1}, confirming that the acidic hydrogen bond donor esterified with the surface hydroxyl groups of cellulose. XRD analysis confirmed that all residual solid samples retained the cellulose I crystal structure (Figure 5c). The crystallinity index (CrI) changes during DES treatment are driven by two competing effects, as shown in Figure 5d. The preferential removal of amorphous lignin and hemicellulose raises CrI, lifting the value from 52.1% in raw poplar wood to 59.5%,

56.7%, 56.1%, and 54.8% for FCR, ACR, LCR, and OCR, respectively. As DES acidity increases, higher proton concentrations intensify acid hydrolysis of exposed crystalline cellulose, disrupting its lattice and shrinking crystallite size. This degradative effect outweighs the CrI-boosting gain from deeper delignification, causing CrI to decrease progressively across the treatment groups.

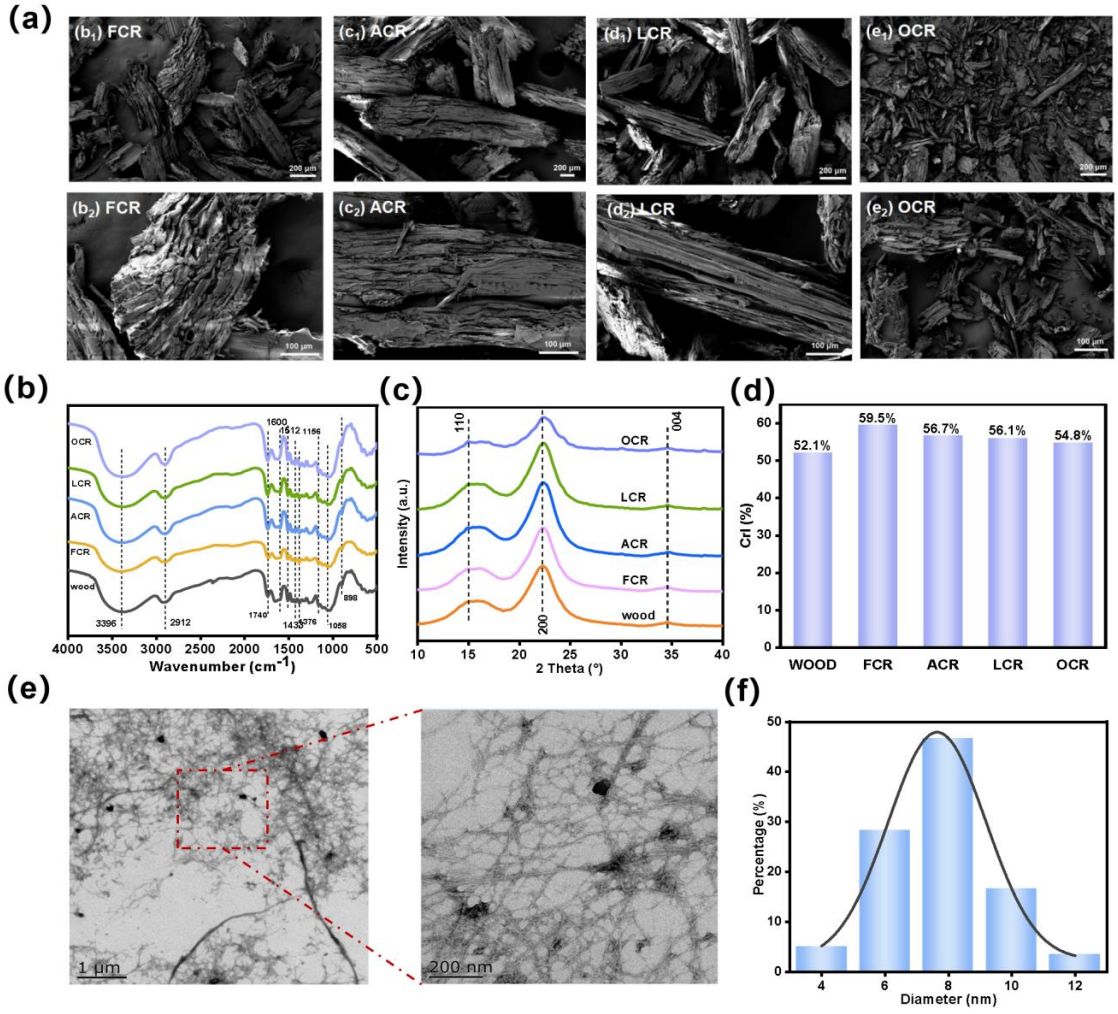


Figure 5. Infrared spectra (a), XRD patterns (b), and crystallinity (c) of cellulose residues, and surface morphologies of FCR, ACR, LCR, and OCR.

Owing to the effective disruption of the LCC structure by the OD system, the depolymerized cellulose residue (OCR) could be readily processed into lignin-containing cellulose nanofibers via high-pressure homogenization. TEM images revealed that the homogenized fibers exhibited a nanoscale elongated fibrous structure (Figure 5e). And statistical analysis showed that the diameter distribution of the LCNF exhibited an approximately normal distribution, with an average diameter

of 7.64 nm (Figure 5f). This is comparable to values reported in the literature [27]. This fibrillation was mainly driven by the high-speed shear, intense collision, and cavitation effects generated during homogenization, which effectively disrupted the interfibrillar interactions and promoted microfibrillation [28]. Meanwhile, the amorphous region structure was disrupted, thereby increasing CrI to 86% (Figure S4). Additionally, the irregular nanoparticles observed in the TEM images likely originated from residual lignin on the fiber surface. FTIR spectrum of LCNF displayed the characteristic peaks of aromatic skeleton at 1500, 1453, and 1428 cm^{-1}, verifying the presence of residual lignin in the LCNF (Figure S5). XPS was performed to characterize the surface chemistry of the LCNFs. The high-resolution C1s spectrum was deconvoluted into three peaks at binding energies of approximately 284.8, 286.5, and 288.0 eV, corresponding to C-C/C=C/C-H, C-O/C-O-C, and O-C-O/C=O, respectively, which might be attributed to the esterification of LCNF and the presence of residual lignin (Figure S6). Collectively, these results demonstrate that OD-mediated depolymerization of lignocellulose not only enables efficient nanofibrillation but also yields LCNF with lignin-enriched surfaces, offering a promising strategy for the value-added utilization of cellulose residues.

3.4 Depolymerization mechanism

The preceding results confirmed that OD could depolymerize lignocellulose through the cleavage of glycosidic bonds in cellulose, ether bonds in lignin, and competitive hydrogen-bond disruption, thereby enabling lignin dissolution and cellulose separation (Figure 6a). However, the specific cleavage sites and reaction pathways of lignin depolymerization remained unclear. To address this, a typical *β-O-4* lignin dimer, guaiacylglycerol-*β*-guaiacyl ether (GBG), was selected as a model compound, which contained the key structural features of lignin, including *β-O-4* linkages, aromatic rings, methoxy groups, and hydroxyl groups. The hydrogen bond topological networks of the OD and GBG, along with their key bond critical points (BCPs), were investigated using DFT simulations (Figure 6b). For OD, the primary interaction was between chloride ions (Cl^-) and hydrogen bond donors, i.e., Cl•••H-O, and the hydrogen bond strength at the Cl•••H-O interactions ranged from $0.0283<\rho<0.0490$ au, while that of the lignin model compound (O•••H-O type

network) ranged from $0.0249<\rho<0.0261$ au (Table S2). The superior hydrogen-bond competition capability of OD thus constituted the basis for the efficient depolymerization of lignin. Another core mechanism underlying lignin depolymerization was the cleavage of ether bonds. As shown in Figure 6c, DFT simulation of GBG revealed that the principal covalent bonds in lignin exhibited bond dissociation energies of 55.85 kcal/mol for the C-O bond and 65.26 kcal/mol for the C-C bond. With the lower dissociation energy, C-O bond was unstable under acidic conditions. The Kamlet-Taft solvatochromic parameters (**Section 3.1**) confirmed that OD possessed stronger acidity and higher hydrogen-bond acidity, which enabled the system to provide a higher concentration of free protons that could closely interact with lignin. During this process, the γ-hydroxyl group (γ-OH) on the lignin side chain was acylated by the carboxylic acid component (-COOH) of the DES, yielding a γ-esterified structure. Subsequently, the acidic protons released from the HBD electrophilically attacked the ether oxygen, leading to C-O bond cleavage (Figure 6d). Quantitative 2D NMR analysis had already confirmed the cleavage mechanism, as reflected by the substantial decrease in *β-O-4* ether linkage units in ODL. Additionally, pronounced signals attributable to S′ units (oxidized syringyl structures) were observed in the 2D HSQC spectra of the depolymerized lignin (Figure 4), providing direct evidence for the enol ether-mediated cleavage. Specifically, protons in the acidic DES attack the α-hydroxyl group (α-OH) in the *β-O-4* structure, leading to the elimination of a water molecule (H_2O) and the formation of a stable carbocation intermediate. Subsequently, an elimination reaction occurs between the positively charged carbocation at the α-position and the adjacent *β*-H atom, generating a key enol ether intermediate (Figure 6d) [29].

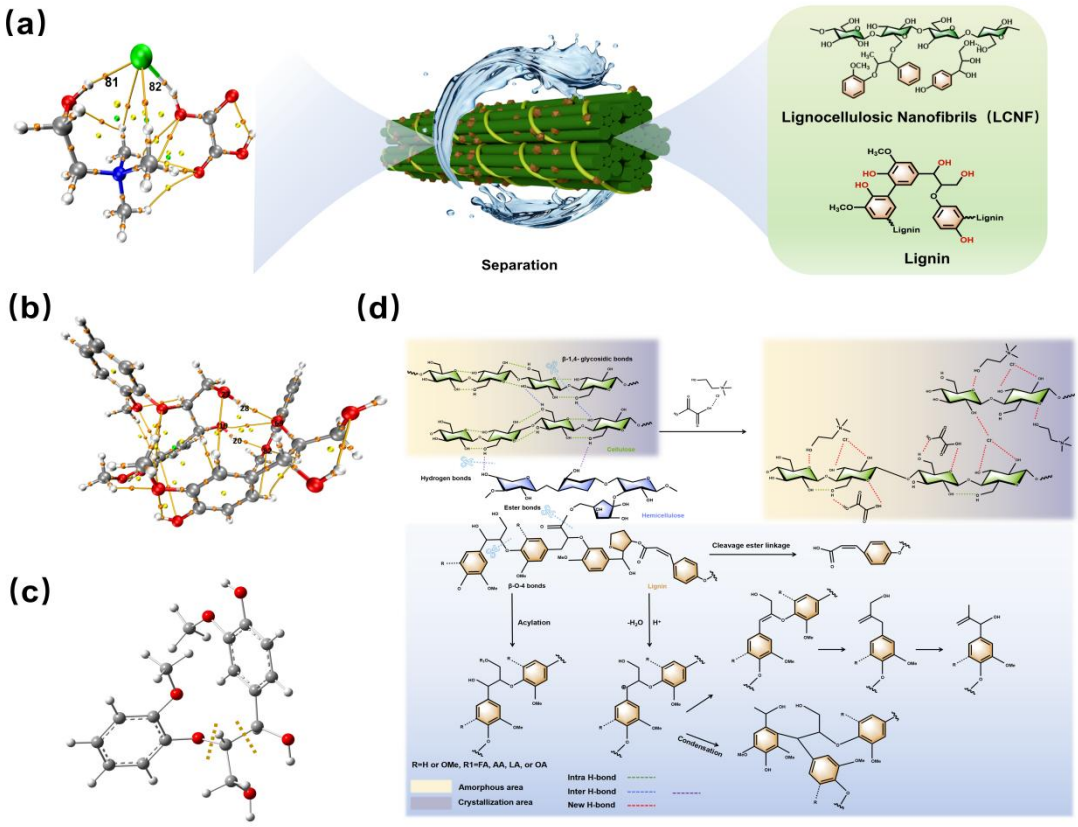


Figure 6. Schematic diagram of LCNF depolymerization (a). Molecular model of GBD (b) and molecular interaction model of GBD-GBD (c). Schematic diagram of the mechanism of lignocellulose depolymerization by deep eutectic solvent (d).

For cellulose, the competitive hydrogen bonding between chloride ions (Cl^-) of choline chloride and hydroxyl groups of the lignin-carbohydrate complex facilitated the cleavage of resistant covalent linkages, including lignin-hemicellulose ester bonds and a portion of β-1,4-glycosidic bonds in cellulose. Meanwhile, OD also disrupted the intra-and intermolecular hydrogen bonds of cellulose, leading to partial depolymerization of the amorphous regions. This selective disruption increased cellulose crystallinity, thereby enhancing its accessibility and facilitating the preparation of lignocellulosic nanofibers (Figure 6d). In summary, the efficient hydrogen bond competition and covalent cleavage synergistic mechanism of OD ensure the synchronous transformation of high-quality lignin and LCNF.

3.5 Large-scale conversion of lignocellulose

Oxalic acid-based DES, based on a chemo-physical synergistic effect, is effective for lignocellulose depolymerization and can be applied to the balanced conversion of

its multicomponents. However, scaling up this process from the laboratory to an industrial scale presents considerable challenges. In this work, an integrated route was designed, covering lignocellulose depolymerization, lignin separation and purification, and LCNF post-treatment, with a batch capacity of 100 kg of lignocellulose. As shown in Figure 7, the OD-treated lignocellulose was converted into a depolymerized slurry, from which the solid residue and the lignin-containing liquor were separated via tubular centrifugation at a rotational speed of 10,000 rpm. The separated liquor was then subjected to precipitation in a settling tank by mixing with deionized water at a liquor-to-water volume ratio of 1:8. The resulting precipitate was filtered and thoroughly washed to obtain purified lignin. Meanwhile, the solid residue, after washing and homogenization, was processed into LCNF by a high-pressure homogenizer operated at 500 bar for three passes. The purified lignin obtained from this integrated process exhibited a hydroxyl group content of 12.4%, and the morphology of the homogenized LCNF was consistent with that of the lab-scale products (Figure S7).

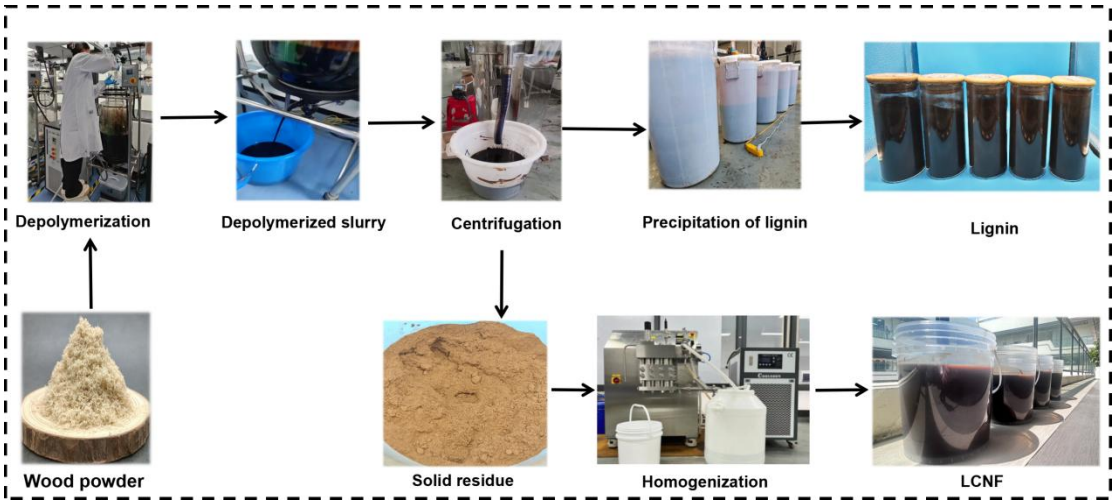


Figure 7. Scalability validation of OD-mediated lignocellulose depolymerization.

Scale-up conversion trials demonstrated that processing 100 kg of wood powder yielded approximately 21.8 kg of lignin and 2205 L of LCNF suspension with a solid content of 2 wt%. The cost analysis is presented in Table S3. The estimated cost for treating of poplar powder was approximately 98.9 CNY/kg, among which DES consumption represented the dominant contribution (81.7%). Significantly, based on our previous study, the oxalic acid-based DES can be readily recycled for five cycles via vacuum distillation [18]. Applying this recycling strategy reduced the overall

conversion cost by 68.7% to 31.0 CNY/kg of biomass, highlighting the economic potential of DES-based lignocellulose fractionation (Figure S8). These findings suggest that significant cost savings can be achieved through multiple reuse cycles. Future efforts will focus on systematically optimizing the large-scale recovery and recycling process of the DES.

Conclusions

To achieve efficient separation and balanced conversion of both lignin and cellulose from lignocellulosic biomass, a series of acidic DESs were designed based on choline chloride as the hydrogen-bond acceptor and various organic acids (lactic, oxalic, formic, and acetic) as hydrogen-bond donors. Kamlet-Taft solvatochromic parameters and density functional theory (DFT) analysis were employed to characterize the four DES systems. The results confirmed that the choline OD system showed the strongest hydrogen-bond acidity (α= 1.882), the shortest hydrogen-bond distance (1.908 Å), the most negative electrostatic potential (-51.32 kcal/mol), and the lowest band gap (4.406 eV). Under such acidic conditions, OD drives efficient removal of lignin and hemicellulose through a dual mechanism: proton-mediated cleavage of covalent bonds and chloride-induced competition for hydrogen bonds. This yielded a lignin extraction rate of 63.3%, with high purity nearly 100%, a phenolic hydroxyl content of 11%, and a relatively low molecular weight of 2038 Da. Meanwhile, the pretreated cellulosic substrate (OCR) exposed substantially more disordered fibrillar structures, allowing its conversion into LCNFs with a crystallinity index of 86% and a diameter of 7.64 nm. The technology has already passed pilot-scale verification at a throughput of 100 kg per day, reinforcing its promise as a green biorefinery process suitable for industrial scaling.

Author contributions

Dengfeng Wang: Writing-original draft, methodology, investigation, formal analysis. **Haojie Hong**: Visualization, validation, formal analysis, data Curation. **Han Wu**: Visualization, validation, formal analysis. **Lin Liu** and **Juming Yao**: Writing-review and editing, project administration, funding acquisition, conceptualization.

Conflicts of interest

The authors declare no competing financial interest.

Acknowledgements、Acknowledgements

The work was financially supported by the National Natural Science Foundation of China (22375181, 22475191), and China Postdoctoral Science Foundation (2025M770130).

References

[1] L. Reyes, L. Abdelouahed, C. Mohabeer, J.C. Buvat, B. Taouk (2021) Energetic and exergetic study of the pyrolysis of lignocellulosic biomasses, cellulose, hemicellulose and lignin. Energy Convers Manage. 244: 114459. https://doi.org/10.1016/j.enconman.2021.114459

[2] J.Y. Cheng, T.J. Chen, X.L. Zhou, H.Y. Bian, C.X. Huang, G.G. Fang, C. Huang (2025) Diol-deep eutectic solvent lignocellulosic fractionation for producing lignin microspheres: Influence of the lignin modification and lignocellulose type on their processes. Chem Eng J 514: 163099. https://doi.org/10.1016/j.cej.2025.163099

[3] S.R. Choi, J.M. Lee (2026) Optimization of kneading parameters for lignocellulose fibrillation. Bioresour Technol 448: 134297. https://doi.org/10.1016/j.biortech.2026.134297

[4] R. Di Sabatino, S.R.A. Kersten, J.P. Lange, M.P. Ruiz (2024) Lignocellulosic biomass to glycols: Simultaneous conversion of cellulose, hemicellulose and lignin using an organic solvent. Biomass Bioenerg 187: 107307. https://doi.org/10.1016/j.biombioe.2024.107307

[5] Y. Liyanage, S. Kim, N. Karanwal, J. Kim (2025) Enhanced production of phenolic monomers from lignocellulose via a two-step depolymerization strategy and solvent system optimization. Energy 338: 138636. https://doi.org/10.1016/j.energy.2025.138636

[6] L.X. Gong, D.N. Feng, J. Liu, Y.H. Yu, J. Wang (2022) Ionic liquid depolymerize the lignocellulose for the enzymatic extraction of feruloylated oligosaccharide from corn bran. Food Chem X 15: 100381. https://doi.org/10.1016/j.fochx.2022.100381

[7] J. Schultz, M. Scherzinger, T. Steinbrecher, A. Isci, M. Kaltschmitt (2025)

Influence of vapothermal and hydrothermal pre-treatment on anaerobic degradability of lignocellulosic biomass. Bioresour Technol 426: 132329. https://doi.org/10.1016/j.biortech.2025.132329

[8] L.F. Long, D.Q. He, T. Zhang, X.X. Chen, X.Z. Meng, A.J. Ragauskas, C. Huang (2025) Unlocking the effects of acid/alkali-catalyzed glycerol organosolv pretreatment on lignocellulosic biorefinery: Substrate digestibility and high-quality lignin. Bioresour Technol 421: 132203. https://doi.org/10.1016/j.biortech.2025.132203

[9] Q. Wu, Y.X. Zhang, L. Zhao, Z.M. Wei, C.H. Song, C.L. Pang, X.J. Pang (2025) Strategies for efficient degradation of lignocellulose from straw: Synergistic effects of acid-base pretreatment and functional microbial agents in composting. Chem Eng J 508: 161048. https://doi.org/10.1016/j.cej.2025.161048

[10] W.M. Li, H. Yuan, Y. Hu, S.H. Dou, E.Z. Zhang, Q. Wu, F.B. Sun (2025) Construction of new thermostable MtLPMO9V in synergism with cellulases for efficient lignocellulosic hydrolysis. Bioresour Technol 430: 132594. https://doi.org/10.1016/j.biortech.2025.132594

[11] G.J. Song, W.H. Hu, E.Z. Zhang, V.K. Gupta, Q. Wu, M. Madadi, C.H. Sun, F.B. Sun (2025) Polyethylene glycol-driven lignin-first biorefinery: A pathway for efficient conversion of lignocellulose to ethanol, furfural, and lignin-derived solid electrolytes. Chem Eng J 515: 163530. https://doi.org/10.1016/j.cej.2025.163530

[12] X.J. Shen, R.C. Sun (2021) Recent advances in lignocellulose prior-fractionation for biomaterials, biochemicals, and bioenergy. Carbohydr Polym 261: 117884. https://doi.org/10.1016/j.carbpol.2021.117884

[13] F. Brienza, D. Cannella, D. Montesdeoca, I. Cybulska, D.P. Debecker (2024) A guide to lignin valorization in biorefineries: Traditional, recent, and forthcoming approaches to convert raw lignocellulose into valuable materials and chemicals. RSC Sustainability 2(1): 37-90. https://doi.org/10.1039/d3su00140g

[14] Y.Z. Liu, N. Deak, Z.W. Wang, H.P. Yu, L. Hameleers, E. Jurak, P.J. Deuss, K. Barta (2021) Tunable and functional deep eutectic solvents for lignocellulose valorization. Nat Commun 12(1): 5424.

https://doi.org/10.1038/s41467-021-25117-1

[15] G.Z. Wu, Y. Cheng, C.X. Huang, C. Yong, Y. Fu (2025) Deep eutectic solvent engineering: a novel ternary system for efficient lignocellulose extraction. Green Chem 27(5): 1556-1569. https://doi.org/10.1039/d4gc05138f

[16] Q.L. Wang, J.Q. Chen, X.Y. Jiang, C. Huang, J. Hayashi, X.Z. Meng, Y.F. Zhou (2026) Process intensification technology-assisted deep eutectic solvent pretreatment for fractionation of lignocellulosic biomass: A review. Green Chem 28(26): 10807-10833. https://doi.org/10.1039/d6gc01236a

[17] Y. Wang, W.J. Zhang, J.Y. Yang, M.F. Li, F. Peng, J. Bian (2022) Efficient fractionation of woody biomass hemicelluloses using cholinium amino acids-based deep eutectic solvents and their aqueous mixtures. Bioresour Technol 354: 127139. https://doi.org/10.1016/j.biortech.2022.127139

[18] D.F. Wang, L. Liu, R.S. Shen, Y.L. Chen, M.Y. Diao, J.M. Yao (2023) Fascinating polyphenol lignin extracted from sawdust via a green and recyclable solvent route. Int J Biol Macromol 234: 123780 . https://doi.org/10.1016/j.ijbiomac.2023.123780

[19] L. Gong, H. Fu, L. Liu, Z. Li, J.Q. Guo, Z. Cao, J.M. Yao (2022) Construction and performance of a nanocellulose-graphene-based humidity sensor with a fast response and excellent stability. ACS Appl Polym Mater 4(5): 3656-3666. https://doi.org/10.1021/acsapm.2c00188

[20] M. Zhou, O.A. Fakayode, A.A. Yagoub, Q.H. Ji, C.S. Zhou (2022) Lignin fractionation from lignocellulosic biomass using deep eutectic solvents and its valorization. Renew Sustain Energy Rev 156: 111986. https://doi.org/10.1016/j.rser.2021.111986

[21] J.H. Sanders, P. Tiller, S.M. Cho, R. Venditti, S. Park (2025) The influence of solvent properties and biomass feedstock characteristics on deep eutectic solvent mediated lignin and hemicellulose fractionation. Int J Biol Macromol 320: 146086. https://doi.org/10.1016/j.ijbiomac.2025.146086

[22] Z. Zhang, P.L. Lv, H.R. Ji, X.X. Ji, Z.J. Tian, J.C. Chen (2024) Functional deep eutectic solvent for lignocellulose valorization via lignin stabilization and cellulose functionalization. Green Chem 26(6): 3453-3465.

https://doi.org/10.1039/d3gc04749k

[23] Q.Q. Xia, C.J. Chen, Y.G. Yao, J.G. Li, S.M. He, Y.B. Zhou, T. Li, X.J. Pan, Y. Yao, L.B. Hu (2021) A strong, biodegradable and recyclable lignocellulosic bioplastic (vol 4, pg 627, 2021). Nat Sustain 4(9): 830-830. https://doi.org/10.1038/s41893-021-00771-x

[24] U. Shakeel, X.L. Li, B.A. Wang, F.H. Geng, M.S.U. Rehman, K. Zhang, J. Xu (2022) Structural characterizations of lignins extracted under same severity using different acids, Int J Biol Macromol 194: 204-212. https://doi.org/10.1016/j.ijbiomac.2021.11.171

[25] J.J. Hao, H.F. Chen, C.Q. Zhang, H.L. Li, X.F. Chen, Z. Xiong, C. Wang, H.J. Guo, H.R. Zhang, L. Xiong, S.S. Yu, X.D. Chen (2025) Reducing lignin condensation and enhancing enzymatic hydrolysis of wheat straw by low-concentration p-toluenesulfonic acid pretreatment assisted with polyethylene glycol. Chem Eng J 511: 162012. https://doi.org/10.1016/j.cej.2025.162012

[26] F. Zhang, Q.X. Lin, W. Lan, J.B. Huang, Z.H. Su, F.X. Yue, C.F. Liu (2025) Natural amino acid-tailored deep eutectic solvents for comprehensive bamboo valorization under mild conditions. Chem Eng J 525 170319. https://doi.org/10.1016/j.cej.2025.170319

[27] X.R. Liu, Y.D. Li, C.M. Ewulonu, J. Ralph, F. Xu, Q.L. Zhang, M. Wu, Y. Huang (2019) Mild alkaline pretreatment for isolation of native-like lignin and lignin-containing cellulose nanofibers (LCNF) from crop waste. ACS Sustain Chem Eng 7(16) : 14135-14142. https://doi.org/10.1021/acssuschemeng.9b02800

[28] L.X. You, B. Marcolini, J. Bour, P. Grysan, Y. Fleming, P. Fischer, C. Soukoulis (2025) Physicochemical, morphological, and rheological properties of cellulose nanofibrils produced via ultra-high-pressure homogenization. Carbohydr Polym Tech 9: 100635. https://doi.org/10.1016/j.carpta.2024.100635

[29] S. Hong, X.J. Shen, Z.M. Xue, Z.H. Sun, T.Q. Yuan (2020) Structure-function relationships of deep eutectic solvents for lignin extraction and chemical transformation. Green Chem 22(21): 7219-7232. https://doi.org/10.1039/d0gc02439b

Supplementary Files

This is a list of supplementary files associated with this preprint. Click to download.

- SupportingInformation.docx